Check for updates

Information-weighted constrained regularization for particle size distribution recovery in multiangle dynamic light scattering

MIN XU,[1] JIN SHEN,[1,*] JOHN C. THOMAS,[1,2] YU HUANG,[1] XINJUN ZHU,[3] LUIS A. CLEMENTI,[4] AND JORGE R. VEGA[4]

[1]*School of Electrical and Electronic Engineering, Shandong University of Technology, Zibo 255049, China*
[2]*Group Scientific Pty Ltd, 23 Pine Lodge Crescent, Grange, SA 5022, Australia*
[3]*The Key Laboratory of Advanced Electrical Engineering and Energy Technology, Tianjin Polytechnic University, Tianjin 300387, China*
[4]*Institute of Technological Development for the Chemical Industry (INTEC, UNL-CONICET), Güemes 3450, Santa Fe 3000, Argentina*
[*]*shenjin@sdut.edu.cn*

Abstract: In particle size measurement with dynamic light scattering (DLS), it is difficult to get an accurate recovery of a bimodal particle size distribution (PSD) with a peak position ratio less than ~2:1, especially when large particles (>350nm) are present. This is due to the inherent noise in the autocorrelation function (ACF) data and the scarce utilization of PSD information during the inversion process. In this paper, the PSD information distribution in the ACF data is investigated. It was found that the initial decay section of the ACF contains more information, especially for a bimodal PSD. Based on this, an information-weighted constrained regularization (IWCR) method is proposed in this paper and applied in multiangle DLS analysis for bimodal PSD recovery. By using larger (or smaller) coefficients for weighting the ACF data, more (or less) weight can then be given to the initial part of the ACF. In this way, the IWCR method can enhance utilization of the PSD information in the ACF data, and effectively weaken the effect of noise at large delay time on PSD recovery. Using this method, bimodal PSDs (with nominal diameters of 400:608 nm, 448:608 nm, 500:600 nm) were recovered successfully from simulated data and it appears that the IWCR method can improve the recovery resolution for closely spaced bimodal particles. Results of the PSD recovery from experimental DLS data confirm the performance of this method.

References and links

1. A. Jillavenkatesa, S. J. Dapkunas, and L. S. H. Lum, *Particle Size Characterization* (Helsingin Yliopisto, 2001).
2. I. D. Morrison, E. F. Grabowski, and C. A. Herb, "Improved techniques for particle size determination by quasi-elastic light scattering," Langmuir **1**(4), 496–501 (1985).
3. R. Foord, E. Jakeman, C. J. Oliver, E. R. Pike, R. J. Blagrove, E. Wood, and A. R. Peacocke, "Determination of diffusion coefficients of haemocyanin at low concentration by intensity fluctuation spectroscopy of scattered laser light," Nature **227**(5255), 242–245 (1970).
4. E. Gulari, E. Gulari, Y. Tsunashima, and B. Chu, "Photon correlation spectroscopy of particle distributions," J. Chem. Phys. **70**(8), 3965–3972 (1979).
5. P. G. Cummins and E. J. Staples, "Particle size distributions determined by a "multiangle" analysis of photon correlation spectroscopy data," Langmuir **3**(6), 1109–1113 (1987).
6. G. Bryant and J. C. Thomas, "Improved particle size distribution measurements using multiangle dynamic light scattering," Langmuir **11**(7), 2480–2485 (1995).
7. G. Bryant, C. Abeynayake, and J. C. Thomas, "Improved particle size distribution measurements using multiangle dynamic light scattering. 2. refinements and applications," Langmuir **12**(26), 6224–6228 (1996).

8. J. R. Vega, L. M. Gugliotta, V. D. G. Gonzalez, and G. R. Meira, "Latex particle size distribution by dynamic light scattering: novel data processing for multiangle measurements," J. Colloid Interface Sci. **261**(1), 74–81 (2003).
9. R. Buttgereit, T. Roths, J. Honerkamp, and L. B. Aberle, "Simultaneous regularization method for the determination of radius distributions from experimental multiangle correlation functions," Phys. Rev. E Stat. Nonlin. Soft Matter Phys. **64**(4), 041404 (2001).
10. L. M. Gugliotta, J. R. Vega, and G. R. Meira, "Latex particle size distribution by dynamic light scattering: computer evaluation of two alternative calculation paths," J. Colloid Interface Sci. **228**(1), 14–17 (2000).
11. S. W. Provencher, "A constrained regularization method for inverting data represented by linear algebraic or integral equations," Comput. Phys. Commun. **27**(3), 213–227 (1982).
12. S. W. Provencher, "CONTIN: A general purpose constrained regularization program for inverting noisy linear algebraic and integral equations," Comput. Phys. Commun. **27**(3), 229–242 (1982).
13. L. A. Clementi, J. R. Vega, L. M. Gugliotta, and H. R. B. Orlande, "A Bayesian inversion method for estimating the particle size distribution of latexes from multiangle dynamic light scattering measurements," Chemometr. Intell. Lab. **107**(1), 165–173 (2011).
14. M. Naiim, A. Boualem, C. Ferre, M. Jabloun, A. Jalocha, and P. Ravier, "Multiangle dynamic light scattering for the improvement of multimodal particle size distribution measurements," Soft Matter **11**(1), 28–32 (2015).
15. L. M. Gugliotta, G. S. Stegmayer, L. A. Clementi, V. D. G. Gonzalez, R. J. Minari, J. R. Leiza, and J. R. Vega, "A neural network model for estimating the particle size distribution of dilute latex from multiangle dynamic light scattering measurements," Part. Part. Syst. Charact. **26**(1-2), 41–52 (2009).
16. H. Ruf and B. J. Gould, "Size distributions of chylomicrons from human lymph from dynamic light scattering measurements," Eur. Biophys. J. **28**(1), 1–11 (1998).
17. H. Ruf, "Effects of experimental errors in dynamic light scattering data on the results from regularized inversions," Prog. Colloid Polym. Sci. **115**, 255–258 (2000).
18. X. Zhu, J. Shen, and L. Song, "Accurate retrieval of bimodal particle size distribution in dynamic light scattering," IEEE Photonics Technol. Lett. **28**(3), 311–314 (2016).
19. M. G. Rasteiro, C. C. Lemos, and A. Vasquez, "Nanoparticle Characterization by PCS: The Analysis of Bimodal Distributions," Particul. Sci. Technol. **26**(5), 413–437 (2008).
20. J. C. Thomas, "Photon correlation spectroscopy: technique and instrumentation," Proc. SPIE **1430**, 2–18 (1991).
21. T. Provder, *Particle Size Distribution: Assessment and Characterization*, (ACS Symposium Series, 1987).
22. G. Mie, "Contributions to the optics of turbid media, especially colloidal metal solutions," Ann. Phys. **25**, 377–445 (1908).
23. J. Shen, J. C. Thomas, X. Zhu, and Y. Wang, "Wavelet denoising experiments in dynamic light scattering," Opt. Express **19**(13), 12284–12290 (2011).
24. K. Schatzel, "Noise in photon correlation and photon structure functions," J. Mod. Opt. **30**, 155–166 (1983).
25. K. Schatzel, "Correlation techniques in dynamic light scattering," Appl. Phys. B-Lasers O. **42**, 193–213 (1987).
26. K. Schatzel, *Dynamic Light Scattering*, W. Brown, ed. (Oxford University, 1993).
27. R. Peters, *Dynamic Light Scattering*, W. Brown, ed. (Oxford University, 1993).
28. D. A. Ross and N. Dimas, "Particle Sizing by Dynamic Light Scattering: Noise and distortion in correlation data," Part. Part. Syst. Charact. **1**(2), 62–69 (1993).
29. N. Ostrowiky, D. Sornette, P. Parker, and E. R. Pike, "Exponential-sampling method for light scattering polydisperity analysis," J. Mod. Opt. **28**, 1059–1070 (1981).
30. M. Bertero and E. R. Pike, "Exponential sampling method for Laplace and other dilationally invariant tranforms: II. Examples in photon correlation spectroscopy and Fraunhofer diffraction," Inverse Probl. **7**(1), 21–41 (1991).
31. B. J. Frisken, "Revisiting the method of cumulants for the analysis of dynamic light-scattering data," Appl. Opt. **40**(24), 4087–4091 (2001).
32. A. G. Mailer, P. S. Clegg, and P. N. Pusey, "Particle sizing by dynamic light scattering: non-linear cumulant analysis," J. Phys. Condens. Matter **27**(14), 145102 (2015).
33. A. N. Tikhonov and V. Y. Arsenin, "Solutions of ill-posed problems," Math. Comput. **32**, 491 (1977).
34. A. B. Yu and N. Standish, "A study of particle size distribution," Powder Technol. **62**(2), 101–118 (1990).
35. S. Suparno, K. Deurloo, P. Stamatelopolous, R. Srivastva, and J. C. Thomas, "Light scattering with single-mode fiber collimators," Appl. Opt. **33**(30), 7200–7205 (1994).
36. X. Liu, J. Shen, J. C. Thomas, S. Shi, X. Sun, and W. Liu, "Multiangle dynamic light scattering analysis using angular intensity weighting determined by iterative recursion," Appl. Opt. **51**(7), 846–854 (2012).

1. Introduction

The particle size distribution (PSD) is an important characteristic of many colloidal materials [1]. Dynamic light scattering (DLS) has been widely used in science and industry for measuring the PSD of submicrometer particles [2]. In this technique the autocorrelation function (ACF) of scattered light intensity is measured using the photon correlation spectroscopy (PCS) method [3, 4] and the PSD is determined by analyzing the ACF data. However, inverting the ACF to recover the PSD is a highly ill-posed mathematical problem,

and the results can be variable due to the limited PSD information using the common single angle DLS technique. Noise in the ACF data also reduces the robustness of the PSD recovery.

To improve the accuracy of the PSD recovery, multiangle dynamic light scattering (MDLS), which combines ACF data sets detected at different scattering angles and can provide extra information than single-angle analysis, has been developed [5–8]. Numerous approaches have been proposed to solve the inverse problem based on MDLS. These include the regularization method [9, 10], the CONTIN constrained regularization method [11, 12], Bayesian strategies method [13, 14], and the neural network method [15], for example. These methods generally work well for unimodal PSDs, but less well for bimodal PSDs with a peak position ratio less than ~2:1, although bimodal PSDs with a peak position ratio larger than ~3:1 can be recovered accurately with the CONTIN method [16, 17]. Zhu et al. [18] proposed a weighted constrained regularization (WCR) method, and applied it to single-angle DLS measurements, in which a bimodal PSD with peaks at 200nm and 350nm was successfully recovered giving resolution for a peak position ratio of ~1.7:1, and in spite of considering particle sizes <350nm.

There are two factors that limit acceptable PSD recoveries in DLS: i) the low information content on the PSD in the ACF data; and ii) the unavoidable presence of noise in the ACF data [19]. To overcome these problems, a novel information-weighted constrained regularization (IWCR) method is proposed in this paper, using the distribution of PSD information in the ACF. In this method, the noise and the PSD information in the ACF are considered simultaneously and applied in MDLS analysis ($M = 1, 3, 6$). The results show that there are distinct and significant advantages using this method in MDLS analysis for recovering bimodal PSDs. It appears that this method can effectively reduce the effect of the noise in the ACF data, enhancing the ability to extract PSD information as well as improving the capacity to discriminate the peaks of bimodal distributions. Results of PSD recovery from experimental data support these observations and provide the experimental basis for the feasibility of this method.

2. Basic DLS theory

When a laser beam is focused into a dilute suspension of colloidal particles, light is scattered in all directions. If the scattered light is detected over a small solid angle [20] at a particular angle, it is observed to undergo light intensity fluctuations, which are due to the Brownian motion of the particles. The timescale of the fluctuations relates to the diffusion coefficient of the particles in the medium, which in turn is related to their sizes. The fluctuations are characterized by measuring the ACF of the scattered light intensity [20], as follows:

$$G_\theta^{(2)}(\tau) = \lim_{T_0 \to \infty} \int_0^{T_0} i_\theta(t) \cdot i_\theta(t+\tau) \, dt \bigg/ T_0. \tag{1}$$

where $i_\theta(t)$ and $G_\theta^{(2)}(\tau)$ are the scattered light intensity at the scattering angle θ and the corresponding ACF, respectively. T_0 is the total analysis time and τ is the delay time. In practice, the intensity ACF of scattered light is calculated by Eq. (2), which can be obtained by using a digital correlator.

$$G_\theta^{(2)}(\tau_j) = \lim_{M \to \infty} \sum_{k=1}^{M} i_\theta(\tau_k) \cdot i_\theta(\tau_{k+j}) \bigg/ M. \tag{2}$$

where $G_\theta^{(2)}(\tau_j)$ is the discrete ACF of the scattered light intensity, τ_j the discrete delay time, and M the total number of samples acquired by the correlator.

In DLS, the light intensity ACF is related to the normalized electric field ACF, $g_\theta^{(1)}(\tau_j)$, by the Siegert relationship [20, 21]

$$G_{\theta}^{(2)}\left(\tau_{j}\right)=B\left(1+\beta(\theta)\left|g_{\theta}^{(1)}\left(\tau_{j}\right)\right|^{2}\right). \tag{3}$$

where B is the measured baseline of $G_{\theta}^{(2)}\left(\tau_{j}\right)$, $\beta(\theta)$ (≤ 1) is the instrumental coherence constant, and j ($1\leq j \leq M$) is the channel number.

For a polydisperse system of colloidal particles, the normalized electric field ACF has the form

$$g_{\theta}^{(1)}\left(\tau_{j}\right)=\sum_{i=1}^{N}\exp\left(-\Gamma\left(\theta,d_{i}\right)\cdot\tau_{j}\right)h_{\theta}\left(d_{i}\right). \tag{4}$$

with

$$\Gamma\left(\theta,d_{i}\right)=\frac{16\pi k_{B}Tn_{m}^{2}\left(\lambda_{0}\right)\sin^{2}\left(\theta/2\right)}{3\eta d_{i}\lambda_{0}^{2}}. \tag{5}$$

and

$$h_{\theta}\left(d_{i}\right)=k_{\theta}C_{I\theta}\left(d_{i}\right)f\left(d_{i}\right). \tag{6}$$

where θ, d_i, k_B, T, λ_0, $n_m(\lambda_0)$, and η are the scattering angle, the diameter of spherical particle, the Boltzmann constant, the absolute temperature of the medium, the wavelength of the incident light, the refractive index of the non-absorbing suspending medium, and the viscosity of the dispersing medium, respectively. The decay constant, Γ, of $g_{\theta}^{(1)}\left(\tau_{j}\right)$, can be calculated with the parameters above and Eq. (5) [2, 16]. $C_{I\theta}(d_i)$ is the fraction of the light intensity scattered by a particle of diameter d_i at θ and is calculated by the Mie scattering theory [22], $f(d_i)$ is the discrete PSD which represents the number particle concentration in the range $[d_i, d_{i+1}]$ and the points of the PSD are evenly spaced in the range $[d_{min}, d_{max}]$ with the (chosen) total number N, and $k_{\theta} = 1\big/\sum_{i=1}^{N}C_{I\theta}\left(d_{i}\right)f\left(d_{i}\right)$, is an a priori unknown proportionality constant for each θ.

In vector form, the discrete MDLS model can be written as:

$$\mathbf{g}_{\theta}^{(1)} = k_{\theta}\mathbf{A}_{\theta}\mathbf{f}. \tag{7}$$

where $\mathbf{g}_{\theta}^{(1)}$ ($M \times 1$) is a vector with elements $g_{\theta}^{(1)}\left(\tau_{j}\right)$; $\mathbf{f}$ ($N \times 1$) is a vector with elements $f(d_i)$, $\mathbf{A}_{\theta}$ ($M \times N$) is a kernel matrix corresponding to the measured ACF at the scattering angle θ. The elements of $\mathbf{A}_{\theta}$ are given by

$$\mathbf{A}_{\theta}\left(j,i\right)=\exp\left(-\frac{16\pi k_{B}Tn_{m}^{2}\sin^{2}\left(\theta/2\right)}{3\eta d_{i}\lambda_{0}^{2}}\cdot\tau_{j}\right)C_{I\theta}\left(d_{i}\right). \tag{8}$$

3. Noise in ACF data

Generally, the scattered light signals detected in DLS are weak (usually less than $\sim 10^{-15}$ W) and may be extremely weak when data are recorded for short times or low count rates. Such situations arise in evolving systems or online applications where measurement time may be limited. Although the PCS technique can reduce the noise with time averaging to improve the statistics [23], the noise mixed in the scattered light signals can still make the intensity ACF inversion uncertain. So an understanding of the noise in ACF data is of importance for improving the performance of the DLS.

In 1983, Schatzel analyzed the sources of noise in ACF data [24]. In his classification, there are two types of noise, intensity noise and photon noise [24, 25]. Other types of noises

(e.g., those inherent to the light source) are typically negligible particularly for well-stabilized laser sources. The intensity noise, which can be characterized as Gaussian under certain assumptions, is related to the scattered light signal, while the photon noise, is Poissonian and inherent to the photon counting process. The intensity noise is strongly correlated and may dominate the photon noise after auto-correlation calculation [26, 27] and give rise to an intensity ACF baseline error which causes the estimated electric field ACF data to deviate from the theoretical data, especially at large lag time. In DLS measurement, it is impossible to avoid this distortion although we can get a less biased estimation [28].

Taking the experimental data of sample AE (details in Section 7) as an example, the normalized light intensity and electric field ACF data at 90°, $G(\tau)$ and $g(\tau)$ are shown in the Figs. 1(a) and 1(b) respectively. It can be seen that the effect of noise on fitted data is worse in $G(\tau)$ and $g(\tau)$, especially at large delay time.

To further study the noise in ACF data, wavelet analysis, a common method to extract the noise mixed in noisy data, was used to extract the noise distribution $n_I(\tau)$ and $n_f(\tau)$ from the noisy ACF data $G(\tau)$ and $g(\tau)$ (Figs. 1(c) and 1(d)). The *db3* wavelet, one of *Daubichies* wavelets, was used to compute the detail coefficients vector (***cDg***), via a single-level wavelet decomposition of $G(\tau)$ (or $g(\tau)$) based on a one-dimensional wavelet transform (i.e. *dwt* in MATLAB software). The detail coefficients, substantially the noise distribution $n_I(\tau)$ (or $n_f(\tau)$), were reconstructed with ***cDg*** using the *db3* wavelet and a direct reconstruction function (i.e. *upcoef* in MATLAB software). As shown as Figs. 1(c) and 1(d), it is obvious that the noise in the light intensity ACF is not significantly different at different delay time. However, for the electric field ACF, larger noise occurs at long delay times, as a consequence of square root transformation required to calculate the electric field ACF $g_\theta^{(1)}\left(\tau_j\right)$ from the light intensity ACF $G_\theta^{(2)}\left(\tau_j\right)$, on the basis of Eq. (3).

Actually, the ACF data at small delay times contain the measurement information used for recovery of the PSD, while very little or no PSD information is contained in the ACF data at large delay times [19, 29, 30]. Additionally, at the large delay times, much more noise is mixed in the ACF data than at the small delay times and this seriously affects the PSD recovery. The WCR method, which uses the ACF weighted with the noise distribution, can reduce the effect of noise in ACF data [18], but the lack of the information on closely spaced components in bimodal samples, needed in the PSD recovery, remains a shortcoming.
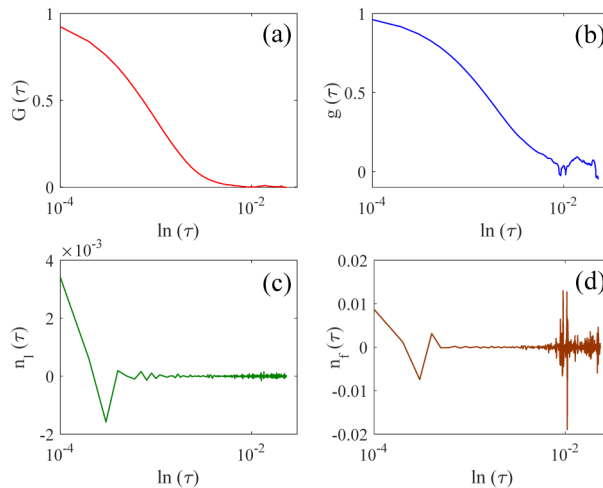
Fig. 1. Normalized light intensity ACF data (a), $G(\tau)$, obtained from experimental sample AE at 90°scattering angle; Normalized electric field ACF data (b), $g(\tau)$, calculated from $G(\tau)$; The noise in $G(\tau)$ (c) and $g(\tau)$ (d), $n_I(\tau)$ and $n_f(\tau)$, extracted by wavelet analysis.

4. PSD information in ACF data

The ACF data contains different amounts of the PSD information at the different delay times, and more PSD information content usually exists at the initial damping section. Generally, the fact of neglecting the PSD information distribution in the common constrained regularization (CR) method or the WCR method, can limit the PSD recovering efficiency.

Here, five simulated DLS data sets with different mean diameter (95nm, 188nm, 350nm, 500nm, 800nm) are used to investigate the PSD information distribution in the ACF data and, the relationship between the PSD information and the recovered PSD. For the simulation, unimodal and bimodal PSDs are used to generate the corresponding ACF data, and the properties of each data set are shown in the Table 1.

All simulations assumed that the particles were dispersed in water at 298 K (refractive index $n = 1.33$, viscosity $\eta = 0.89$ cP). The light source was vertically polarized with wavelength $\lambda_0 = 633$nm. The ACF data were simulated by Eq. (4) at a scattering angle of $\theta = 90°$, adding Gaussian random noise to make the simulated ACF data more realistic.

The noisy light intensity ACF data were simulated by

$$G^{(2)}_{\theta\_noise}\left(\tau_j\right) = G^{(2)}_{\theta}\left(\tau_j\right) + \delta n_1\left(\tau_j\right). \tag{9}$$

where $n_1(\tau_j)$ is the zero-mean Gaussian random noise, and δ denotes the noise standard deviation.

Taking the PSD with a mean diameter of 95nm as an example, a unimodal PSD and three bimodal PSDs (25/300nm 50/200nm 75/125nm), with peak position ratio of 12:1, 4:1 and 1.67:1 respectively, were used to simulate the ACF data. Figure 2(a) shows the simulated light intensity ACF data for the respective PSD. It can be seen that the light intensity ACF data from the 95nm unimodal PSD and the 75/125nm bimodal PSD are quite similar, which makes it highly difficult to discriminate these two sets of light intensity ACF data.

To make the difference between the ACFs more clear, we define the particle size information distribution for bimodal PSDs of Fig. 2(b) as the absolute value of the difference between each datum point of the bimodal ACFs and the ACF corresponding to the equivalent monodisperse PSD (e.g. the 95 nm unimodal ACF in this case). Here, the equivalent monodisperse PSD was obtained by the cumulants method [31, 32]. It can be seen that, as the peak position ratio decreases, the difference between the ACFs decreases and less particle size information is provided as the bimodal PSDs approach a unimodal PSD. So it is increasingly difficult to recover this kind of bimodal PSD.

To illustrate the limitation of the common CR method, the PSD estimations were made by this method and the results are shown in Table 1 and Fig. 2(c). It is easy to see that an accurate recovery of bimodal PSDs was reached when the peak position ratio is > 2:1, such as the 25/300nm and 50/200nm bimodal PSDs, but only one peak was found for the 75/125nm bimodal PSD, with the peak position ratio of 1.67:1.

Simulations were also made for PSDs with different mean diameters (188nm, 350nm, 500nm, 800nm), and the results are shown in Figs. 3-6. In all cases, the less PSD information in the ACF data, the worse the PSD recovery. This effect was particularly evident in the bimodal PSDs with a peak position ratio < 2:1. Clearly, it is critical to make the best use of the PSD information in the ACF data during the inversion to improve the recovery of bimodal PSDs with close peaks.

Table 1. Properties of Simulated ACF Data Sets for the Unimodal and Bimodal PSDs, and a Summary of Particle Sizing Results from Single-angle DLS with a Constrained Regularization Method.

| d_{mean}/nm	d_1/nm	d_2/nm	$d_2{:}d_1$	Intensity Ratio	Noise	Recovered PSDs	
		Simulated PSDs					
95	95	-	-	-		1 peak	V. good
	25	300	12.00:1	0.37:0.63	3×10^{-3}	2 peaks	V. good
	50	200	4.00:1	0.44:0.56		2 peaks	good
	75	125	1.67:1	0.43:0.57		1 peak	poor
188	188	-	-	-		1 peak	V. good
	50	600	12.00:1	0.36:0.64	3×10^{-3}	2 peaks	V. good
	100	450	4.50:1	0.49:0.51		2 peaks	good
	150	300	2.00:1	0.64:0.36		1 peak	poor
350	350	-	-	-		1 peak	V. good
	125	900	7.20:1	0.37:0.63	3×10^{-3}	2 peaks	V. good
	200	800	4.00:1	0.51:0.49		2 peaks	good
	275	600	2.18:1	0.65:0.35		1 peak	poor
500	500	-	-	-		1 peak	V. good
	100	900	9.00:1	0.21:0.79	3×10^{-3}	2 peaks	V. good
	175	700	4.00:1	0.19:0.81		2 peaks	good
	350	600	1.71:1	0.31:0.69		1 peak	poor
800	800	-	-	-		1 peak	V. good
	175	1000	5.71:1	0.10:0.90	3×10^{-3}	2 peaks	V. good
	250	950	3.80:1	0.10:0.90		2 peaks	good
	450	900	2.00:1	0.15:0.85		1 peak	poor
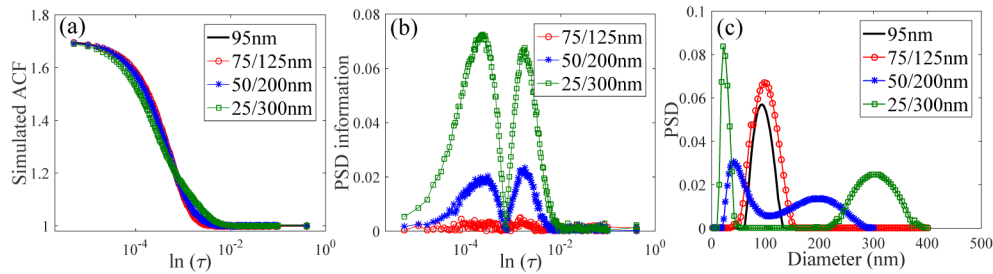
Fig. 2. Simulated light intensity ACF data for the PSDs with 95nm mean diameter (a); PSD information distribution in the simulated ACF data for the bimodal PSDs (b); PSDs estimated from the simulated ACF data by using the common CR method (c).
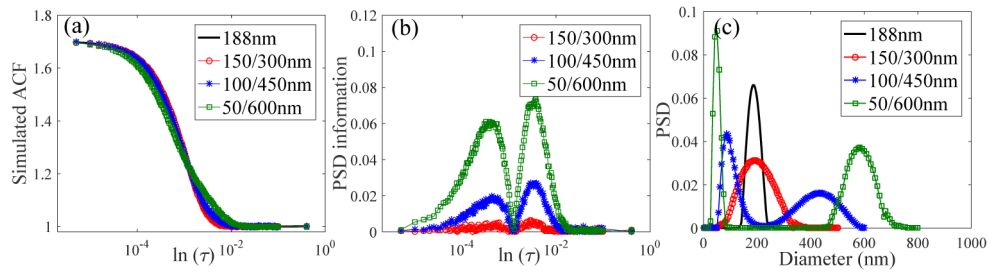
Fig. 3. Simulated light intensity ACF data for the PSDs with 188nm mean diameter (a); PSD information distribution in the simulated ACF data for the bimodal PSDs (b); PSDs estimated from the simulated ACF data by using the common CR method (c).
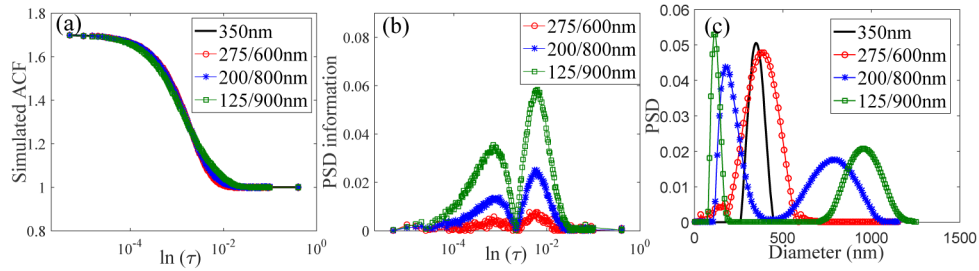

Fig. 4. Simulated light intensity ACF data for the PSDs with 350nm mean diameter (a); PSD information distribution in the simulated ACF data for the bimodal PSDs (b); PSDs estimated from the simulated ACF data by using the common CR method (c).

Fig. 5. Simulated light intensity ACF data for the PSDs with 500nm mean diameter (a); PSD information distribution in the simulated ACF data for the bimodal PSDs (b); PSDs estimated from the simulated ACF data by using the common CR method (c).
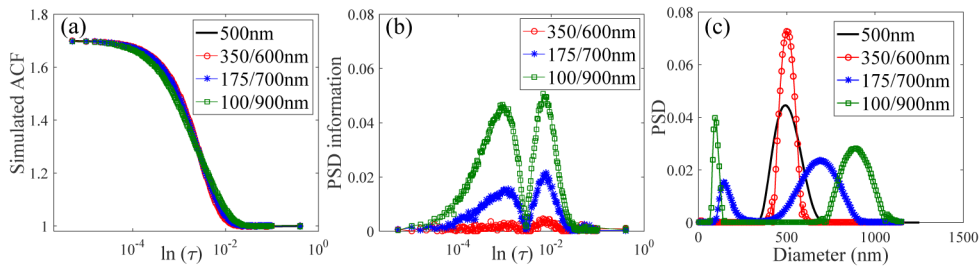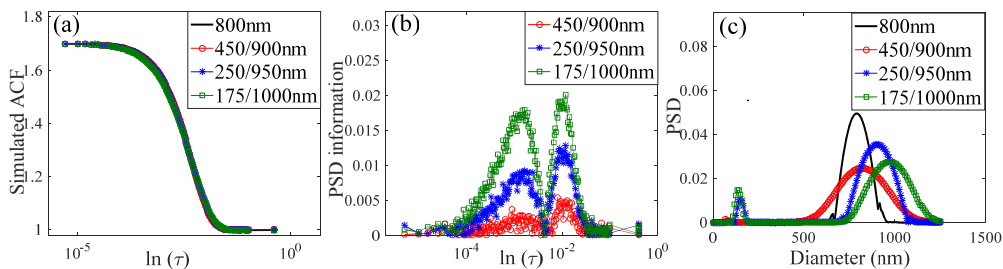

Fig. 6. Simulated light intensity ACF data for the PSDs with 800nm mean diameter (a); PSD information distribution in the simulated ACF data for the bimodal PSDs (b); PSDs estimated from the simulated ACF data by using the common CR method (c).

5. IWCR method

To increase the ability to extract the PSD information, the here-proposed IWCR method is applied in MDLS. This method basically consists on assigning a different weight to each data in the ACF, according to the corresponding information content on the PSD.

For single-angle DLS (SDLS), the IWCR method can be expressed as a weighted constrained optimization problem, as follows:

$$M^{\alpha}\left(\mathbf{f}\right) = \left\| \mathbf{W}_{\theta}\left(\mathbf{A}_{\theta}\mathbf{f} - \mathbf{g}_{\theta}^{(1)} \right) \right\|^{2} + \alpha \left\| \mathbf{L}\mathbf{f} \right\|^{2} \quad , 0 \leq \mathbf{f} \leq 1. \tag{10}$$

where M^{α} is the objective functional to be minimized, $\mathbf{f}$ the estimated PSD, α the regularization parameter, $\mathbf{L}$ the regularization matrix, $\|\cdot\|$ the Euclidean norm, and $\|\mathbf{L}\mathbf{f}\|$ the penalty functional factor. These parameters guarantee the optimal stable and smooth solution.

The weighting matrix $\mathbf{W}_{\theta}$ in Eq. (10), is described by $\mathbf{W}_{\theta} = \mathrm{diag}(\boldsymbol{w}_{\theta})$. Here diag is the diagonal operator and $\boldsymbol{w}_{\theta}$ is a vector of weighting coefficients, w_{θ_j}, that can be calculated by:

$$w_{\theta\_j} = \left| g_{\theta\_j}^{(1)} \right|^{PID_{\theta\_j}/2}. \tag{11}$$

where $g_{\theta\_j}^{(1)}$ is the jth element of $\mathbf{g}_{\theta}^{(1)}$, and PID_{θ_j} is the jth element of the PSD information distribution in the ACF data. This information distribution at scattering angle θ, PID_{θ}, substantially is the absolute value of difference between the ACF corresponding to the equivalent monodisperse PSD and actual ACF. Here, the equivalent monodisperse PSD was obtained by the cumulants method [31, 32].

In the IWCR method, a larger (smaller) value of w_{θ} is generally used to weight the ACF data which has more (less) PSD information. In this way, it is possible to provide more precise PSD information contained in the ACF to improve the PSD recovery. The effect of noise at large delay times is also weakened by using smaller weighting coefficients at those delay times.

In MDLS analysis, the estimated ACF data obtained at different scattering angles is treated as one set. Correspondingly, with IWCR method Eq. (7) is expressed as,

$$\mathbf{g}_{W}^{(1)} = \begin{bmatrix} \mathbf{W}_{1}\mathbf{g}_{\theta_{1}}^{(1)} \\ \mathbf{W}_{2}\mathbf{g}_{\theta_{2}}^{(1)} \\ \vdots \\ \mathbf{W}_{m}\mathbf{g}_{\theta_{m}}^{(1)} \end{bmatrix} = \begin{bmatrix} k_{1}\mathbf{W}_{1}\mathbf{A}_{\theta_{1}} \\ k_{2}\mathbf{W}_{2}\mathbf{A}_{\theta_{2}} \\ \vdots \\ k_{m}\mathbf{W}_{m}\mathbf{A}_{\theta_{m}} \end{bmatrix} \mathbf{f} = \mathbf{A}_{\mathbf{W}}\mathbf{f}. \tag{12}$$

where $\mathbf{g}_{\theta_{r}}^{(1)}$ is the electric field ACF data at scattering angle θ_{r}, $\mathbf{A}_{\theta_{r}}$ is the kernel matrix corresponding to $\mathbf{g}_{\theta_{r}}^{(1)}$, $\mathbf{W}_{r}$ is the weighting matrix corresponding to $\mathbf{g}_{\theta_{r}}^{(1)}$, calculated by Eq. (11), k_{r} is the a priori unknown constant related to the scattering angle θ_{r}, where r is a integer within 1 to m.

Similarly, the PSD recovery with the IWCR method in MDLS can be expressed in a weighted constrained functional optimization form as

$$M^{\alpha}\left(\mathbf{f}\right) = \left\| \mathbf{A}_{\mathbf{W}}\mathbf{f} - \mathbf{g}_{\mathbf{W}}^{(1)} \right\|^{2} + \alpha \left\| \mathbf{L}\mathbf{f} \right\|^{2} \quad , 0 \leq \mathbf{f} \leq 1. \tag{13}$$

where $\mathbf{A}_{\mathbf{W}}$ is the kernel matrix of Eq. (12), $\mathbf{A}_{\mathbf{W}} = [\, k_{1}\mathbf{W}_{1}\mathbf{A}_{\theta_{1}} \,;\, k_{2}\mathbf{W}_{2}\mathbf{A}_{\theta_{2}} \,;\, \ldots;\, k_{m}\mathbf{W}_{m}\mathbf{A}_{\theta_{m}} \,]$, and $\mathbf{g}_{\mathbf{W}}^{(1)}$ is a vector set containing the weighted electric field ACF data at scattering angles $\theta_{1}, \theta_{2}, \ldots, \theta_{m}$, as described by the second member of Eq. (12).

In what follows, the simulated and experimental PSDs are recovered by the proposed IWCR method (W2) with single-angle or multi-angle ACF data and compared with PSDs recovered using the standard CR method (W0) proposed by Tikhonov et al. [33] and the WCR method (W1) proposed by Zhu et al. [18]. The following four indices are used to measure the relative performance of the methods: the peak position (PP), the relative error of peak position (E_{PP}), the peak height ratio of bimodal PSD (R_{PH}), and the rms PSD recovery error (V). The index PP here is the particle diameter at the PSD maximum. The other indices are defined as follows:

$$R_{PH} = HIP_1 / HIP_2$$
$$E_{PP} = \left| \left(PP_{true} - PP_{meas} \right) / PP_{true} \right| \qquad (14)$$
$$V = \left\{ \left(\sum_1^K \left[f_{true}(d) - f_{meas}(d) \right]^2 \right) \middle/ K \right\}^{1/2}.$$

where HIP stands for the value of the PSD at PP; and K is the number of modes in the PSD.

6. Simulation and results

Using a combination of two PSDs from Johnson's S_B distribution [34], a realistic bimodal PSD was simulated as

$$f(d) = a \frac{\sigma_1}{(d_{max} - d_{min})\sqrt{2\pi}} [t(1-t)]^{-1} \exp\left\{ -0.5[u_1 + \sigma_1 \ln(\frac{t}{1-t})]^2 \right\}$$
$$+ b \frac{\sigma_2}{(d_{max} - d_{min})\sqrt{2\pi}} [t(1-t)]^{-1} \exp\left\{ -0.5[u_2 + \sigma_2 \ln(\frac{t}{1-t})]^2 \right\}, \quad (a+b=1). \qquad (15)$$

where $t = (d - d_{min})/(d_{max} - d_{min})$, and μ_1, σ_1, μ_2, σ_2, a, and b are distribution parameters used to get different PSDs. Parameter d is the particle diameter, d_{min} and d_{max} are the maximum and minimum particle diameter respectively, and t is the normalized particle diameter.

The intensity ACF data without noise can be obtained using Eqs. (3) and (4). Three sets of PSD and their corresponding ACF data were simulated with the parameters shown in Tables 2 and 3. Parameters d_1 and d_2 in Table 3 are the diameters at the maximum of each peak. And Gaussian random noise was added to the simulated data to make it more realistic, using the form in Eq. (9). The levels of noise are shown in Table 3.

Table 2. Parameters of Simulated Bimodal Polydisperse PSD Data Sets.

Sample	μ_1	σ_1	μ_2	σ_2	a	b
AS	0.00	8.00	7.90	7.00	0.53	0.47
BS	−2.20	10.00	7.90	7.00	0.53	0.47
CS	3.20	8.00	5.63	13.80	0.65	0.35

Table 3. Properties of Simulated ACF Data Sets for the Bimodal Polydisperse PSDs.

Sample	d_1/nm	d_2/nm	d_2:d_1	R_{PH}	Noise
AS	400	608	1.52:1	1:1.046	3×10^{-3}
BS	448	608	1.36:1	1:0.845	3×10^{-3}
CS	500	600	1.20:1	1:0.921	3×10^{-3}

All ACF data were simulated with $k_B = 1.3807 \times 10^{-23}$ J/K, $T = 298.15$ K, $\eta = 0.89$ cP, $n_m = 1.3316$, $\lambda_0 = 632.8$ nm, $\theta_r = 30°, 40°, 50°, ..., 140°$; $B = 1$, and $\beta = 0.7$; $d_{min} = 0.01$nm and $d_{max} = 800.01$nm for Sample AS and BS, $d_{min} = 300.01$nm and $d_{max} = 800.01$nm for Sample CS. The number of points was 100.

Using M-angle DLS (M = 1, 3, 6), recovery of the simulated PSDs was done by analyzing the noisy simulated ACF data with different constrained regularization methods (W0, W1 and W2). SDLS was simulated at 90°; 3-angle DLS was simulated at 70°, 90° and 110°; 6-angle

DLS was simulated at 30°, 50°, …, 130°. Recovered PSDs are shown in Figs. 7-9, and the values of the different performance indices are shown in Tables 4-6.

For the simulated bimodal PSD containing 400:608 nm spheres with 1:1.046 peak height ratio (sample AS), the recovered PSDs are shown in Fig. 7 separately using single-angle, 3-angle and 6-angle analysis. Table 4 shows the performance indices of the true and recovered PSDs.

According to Fig. 7, a better estimation of the 400nm and 608nm peaks was obtained with the W2 method. Also, the recovered PSDs were closer to the true PSDs with increasing number of scattering angles. The ability to recognize the bimodal PSD of the W0 method was very poor for either SDLS or MDLS, although the latter reach more accurate peak position. Using multi-angle methods, particularly 3-angle analysis, the recovered peak height ratios were closer to the true value (1:1.046) with different inversion methods (particularly, W2), which was 1:1.105. The recovered peak position was also more accurate for both the 400 nm and 608 nm peaks. In fact, their relative errors were 0.023 and 0.006 respectively, when analyzing the 3-angle DLS data with the W2 method.

For the simulated bimodal PSD containing 448:608 nm spheres with a 1:0.845 peak height ratio (sample BS) the recovered PSDs are shown in Fig. 8. Table 5 shows the performance indices of the true and recovered PSDs.

A better estimation of the 448 nm and 608 nm peaks was extracted with 3-angle analysis, especially when using the W2 inversion method. With SDLS, this PSD could not be recovered well when compared with MDLS, particularly using the W0 method. In addition, small, spurious 200 nm and 170 nm peaks were obtained by the W0 or W1 methods in 6-angle DLS. In contrast, the W2 inversion method did not produce these spurious peaks. According to Table 5, better results are obtained when using 6-angle DLS data with the W2 method. Here the relative peak position errors of the 448 nm and 608 nm peaks were 0.026 and 0.006 respectively, the recovered peak height ratio was 1:1.083, and the value of V was 0.067.
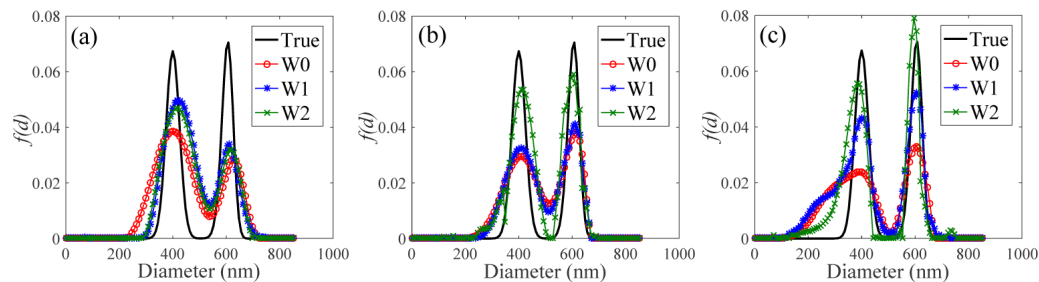

Fig. 7. Simulated and estimated values for Sample AS, a bimodal particle size distribution with peaks at 400 nm and 608 nm. The recovery of PSD is estimated by different constrained regularization methods (W0, W1 and W2) in single-angle DLS (a), three-angle DLS (b) and six-angle DLS (c).
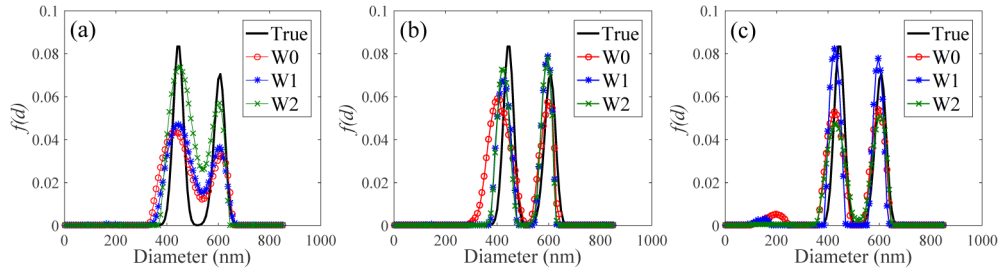
Fig. 8. Simulated and estimated values for Sample BS, a bimodal particle size distribution with peaks at 448 nm and 608 nm. The recovery of PSD is estimated by different constrained regularization methods (W0, W1 and W2) in single-angle DLS (a), three-angle DLS (b) and six-angle DLS (c).
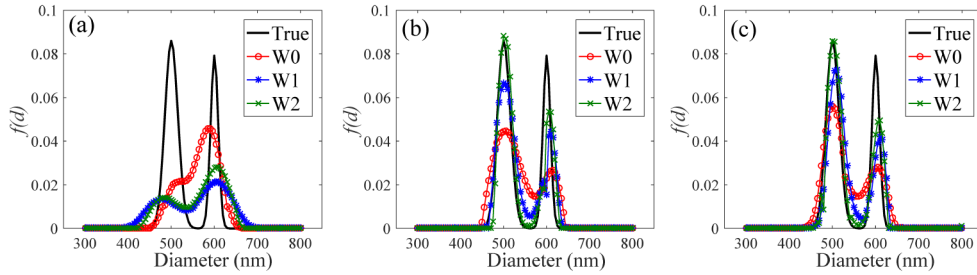

Fig. 9. Simulated and estimated values for Sample CS, a bimodal particle size distribution with peaks at 500 nm and 600 nm. The recovery of PSD is estimated by different constrained regularization methods (W0, W1 and W2) in single-angle DLS (a), three-angle DLS (b) and six-angle DLS (c).

Table 4. Performance indices (PP, E_{PP}, R_{PH} and V) of the true and recovered PSDs for Sample AS.

			PP /nm	E_{PP}	R_{PH}	V
	True PSD		400/608	0.000/0.000	1.000:1.046	0
Recovered PSDs	1-angle DLS	W0	401/630	0.003/0.036	1.000:0.738	0.104
		W1	418/613	0.045/0.008	1.000:0.682	0.095
		W2	417/621	0.042/0.021	1.000:0.684	0.096
	3-angle DLS	W0	409/613	0.023/0.008	1.000:1.287	0.088
		W1	409/613	0.023/0.008	1.000:1.262	0.081
		W2	409/604	0.023/0.006	1.000:1.105	0.067
	6-angle DLS	W0	392/604	0.020/0.006	1.000:1.385	0.099
		W1	401/604	0.003/0.006	1.000:1.206	0.076
		W2	390/596	0.025/0.019	1.000:1.422	0.073

Table 5. Performance indices (PP, E_{PP}, R_{PH} and V) of the true and recovered PSDs for Sample BS.

			PP /nm	E_{PP}	R_{PH}	V
	True PSD		448/608	0.000/0.000	1.000:0.845	0
Recovered PSDs	1-angle DLS	W0	435/613	0.029/0.008	1.000:0.762	0.098
		W1	443/604	0.011/0.006	1.000:0.773	0.088
		W2	451/604	0.007/0.006	1.000:0.773	0.086
	3-angle DLS	W0	401/596	0.105/0.020	1.000:0.968	0.110
		W1	426/596	0.049/0.020	1.000:1.169	0.093
		W2	422/596	0.058/0.019	1.000:1.026	0.100
	6-angle DLS	W0	426/596	0.049/0.020	1.000:1.029	0.076
		W1	426/596	0.049/0.019	1.000:0.905	0.088
		W2	436/604	0.026/0.006	1.000:1.083	0.067

Table 6. Performance indices (PP, E_{PP}, R_{PH} and V) of the true and recovered PSDs for Sample CS

			PP /nm	E_{PP}	R_{PH}	V
	True PSD		500/600	0.000/0.000	1.000: 0.921	0
Recovered PSDs	1-angle DLS	W0	520/590	0.04/0.017	1.000:2.138	0.135
		W1	480/605	0.04/0.008	1.000:1.597	0.132
		W2	485/605	0.03/0.008	1.000:1.975	0.129
	3-angle DLS	W0	505/615	0.01/0.025	1.000:0.598	0.103
		W1	500/610	0.00/0.017	1.000:0.667	0.077
		W2	500/605	0.00/0.008	1.000:0.609	0.060
	6-angle DLS	W0	500/605	0.00/0.008	1.000:0.500	0.082
		W1	510/615	0.02/0.025	1.000:0.558	0.080
		W2	500/610	0.00/0.017	1.000: 0.575	0.056

Figure 9 and Table 6 show the results for the simulated bimodal PSD containing 500:600 nm spheres with a 1:0.921 peak height ratio (sample CS). The PSDs recovered are shown in Fig. 9. In the single angle analysis, there was no significant deference between the recovered PSD with the W1 and W2 method. Obviously the recovered PSDs from these two methods are more close to true PSD than the recovery with W0 method. As increase of the scattering angles, the W2 method could give better recovered PSD, not only than W0 method, but also than W1 method.

The most accurate peak positions were obtained using 3-angle analysis and the W2 method where the relative peak position errors were 0.00 and 0.008 for the 500 nm and 600 nm peaks respectively, and the recovered peak height ratio was 1:0.609, close to the true value 1:0.921.

7. Experimental section

Real experimental data corresponding to three bimodal samples (AE, BE, CE) were used to evaluate the proposed method. Samples AE and BE were both obtained by mixing 306 nm ± 8 nm and 974 nm ± 10 nm standard polystyrene latex spheres (*Polyscience Inc.*), all of which were diluted into the distilled and deionized water. For sample AE, the number concentrations of the small and large particles were 98.95% and 1.05% respectively (which correspond to 50% in weight for each mode). For sample BE, the number concentrations of the small and large particles were 97.90% and 2.10% respectively (which correspond to 34% and 66% in weight for each mode). Sample CE was obtained by mixing 300 nm ± 3 nm and 502 nm ± 4 nm standard polystyrene latex spheres (*Duke Scientific*) in 1mM NaCl in a number ratio of 5:1, based on the manufacturer's nominal concentration. For all bimodal samples, the regulated sample temperature was 298.15 K, and the dispersion medium refractive index (n_m) was 1.33.

MDLS measurements were made with a general purpose laser light scattering photometer (*Brookhaven Instruments, Inc.*), fitted with a 20 mW vertically polarized He–Ne laser (λ_0 = 632.8 nm), a photomultiplier tube as a detector, a stepper-motor controlled goniometer (model BI-200SM, *Brookhaven Instruments Inc.*), and a digital correlator (*Brookhaven Instruments Inc.* model BI-2000 AT for sample AE and BE, model BI-2030AT for sample CE). The intensity ACF data, from sample AE and BE, were recorded at twelve detection angles (R = 12): [30°, 40°, 50°, 60°, 70°, 80°, 90°, 100°, 110°, 120°, 130° and 140°]. For sample CE, the MDLS was carried out in the detection angle range 30° to 120° at intervals of 10°. The angular alignment of the goniometer was checked prior to all measurements. Total measurement times ranged from 200 s to 500 s and a single-mode fiber-optic probe was used to collect the scattered light, which can ensure high-coherence ACF data [35].

As for the simulated bimodal PSDs, the experimental sample PSDs were recovered by *M*-angle DLS (M = 1, 3, 6) analysis with different constrained regularization methods (W0, W1 and W2 method). The SDLS data was obtained at 90° scattering angle; 3-angle DLS data was detected at 70°, 90° and 110°; 6-angle DLS was obtained at 30°, 50°, 70°, 90°, 110°, 130° for sample AE and BE, as well as 30°, 50°, 70°, 90°, 110°, 120° for sample CE. The value of k_r was calculated with the iterative recursion estimation method [36]. Figures 10-12 show the recovered PSDs, and the value of the different performance indices are shown in the Tables 7-9.

For the experimental bimodal PSD containing 306:974 nm spheres with a 1:1 peak height ratio (sample AE), the recovered PSDs are shown in Fig. 10. The different performance indices of the true and recovered PSDs are shown in Table 7. With these values, we can compare the recovery results obtained by different analysis methods.

For the 360 nm and 974 nm peaks, each of the MDLS analyses successfully obtained a good estimation of the PSD with the 6-angle DLS solution being more reliable, especially for the W2 method. Furthermore, the height ratio of the peaks recovered with the W2 method is much closer to the true ratio than with either the W0 or W1 methods. Also the peak positions were more accurate, with relative errors of 0.003 and 0.006 for the 360 nm and 974 nm peaks respectively, when we used 3-angle DLS and the W2 method. The recovered peak height ratio in this case was 1:1.06, very close to the true value of 1:1.

For the bimodal PSD containing 306:974 nm spheres with a 1:2 peak height ratio (sample BE), the recovered PSDs are shown in Fig. 11. The different performance indices are shown in Table 8.

In all cases, a bimodal PSD is extracted but they are all quite different. The recovered peak positions with the W2 method are much closer to the true positions than obtained with the W0 and W1 methods. The PSDs recovered from single-angle analysis resolve the large size peak poorly. In Fig. 11(b) (3-angle MDLS) the recovered PSDs are also poor, but the recovered peak height ratio is much closer to the true value than with SDLS. We can see also that a small, spurious 500 nm peak in the PSD is recovered by the W0 and W1 methods for 3-angle MDLS. Furthermore, 3-angle and 6-angle analysis respectively obtained a closer recovered peak height ratio and a small relative error of peak position, when using the W2 method.

The PSDs, shown in Fig. 12, are the recovery results of the bimodal PSD containing 300:502 nm spheres with a 5:1 peak height ratio (sample CE). The performance indices are shown in Table 9. Clearly, bimodal PSDs are obtained in all cases, but they are all quite different. The recovered peak positions and peak height ratios with the W2 method are all much closer to the true value than obtained with the W0 and W1 methods, especially in the MDLS measurement. The results suggest that the 6-angle DLS solution with the W2 method is more reliable, with smaller relative errors of 0.000 and 0.016 for the 300 nm and 502 nm peaks respectively and a closer peak height ratio of 4.914:1 to the true value of 5:1.
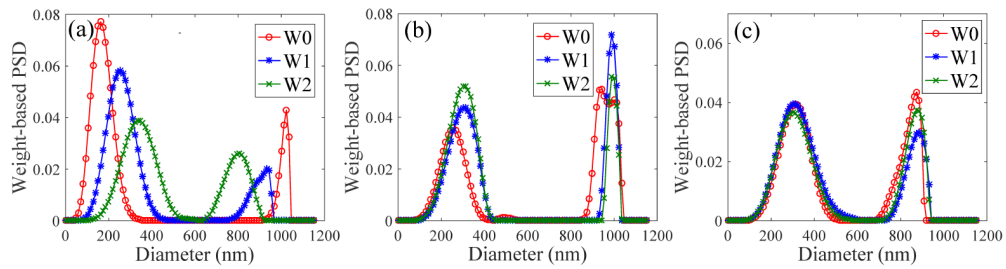
Fig. 10. Estimated particle size distribution for Sample AE, a 306 nm and 974 nm bimodal latex sphere sample mixed in the ratio 1:1, using different constrained regularization methods (W0, W1 and W2) in single-angle DLS (a), three-angle DLS (b) and six-angle DLS (c).
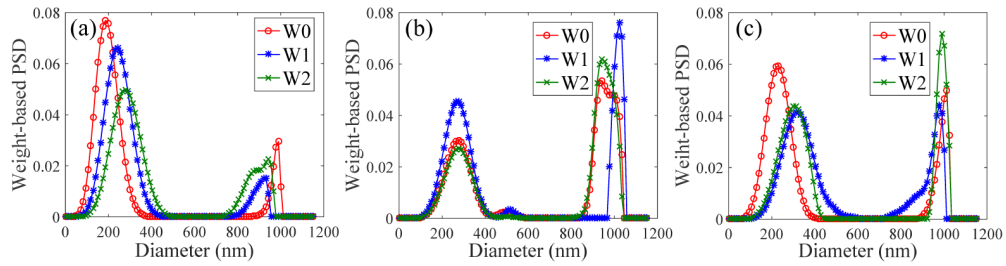

Fig. 11. Estimated particle size distribution for Sample BE, a 306 nm and 974 nm bimodal latex sphere sample mixed in the ratio 1:2, using different constrained regularization methods (W0, W1 and W2) in single-angle DLS (a), three-angle DLS (b) and six-angle DLS (c)
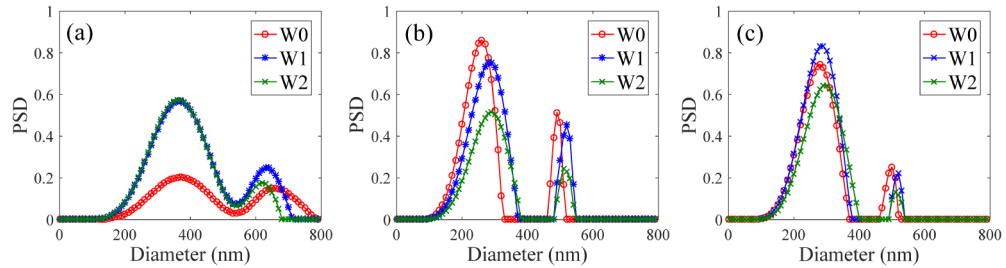

Fig. 12. Estimated particle size distribution for Sample CE, a 300 nm and 502 nm bimodal latex sphere sample mixed in the ratio 5:1, using different constrained regularization methods (W0, W1 and W2) in single-angle DLS (a), three-angle DLS (b) and six-angle DLS (c)

Table 7. Performance indices (*PP*, *E_PP*, and *R_PH*) of the true and recovered PSDs for Sample AE

			PP /nm	*E_PP*	*R_PH*
	True PSD		306/974	0.000/0.000	1.000:1.000
Recovered PSDs	1-angle DLS	W0	163/1024	0.467/0.051	1.000:0.555
		W1	257/935	0.160/0.040	1.000:0.343
		W2	335/811	0.095/0.167	1.000:0.671
	3-angle DLS	W0	255/943/1000	0.167/0.032/0.027	1.000:1.426:1.308
		W1	311/989	0.016/0.015	1.000:1.641
		W2	305/980	0.003/0.006	1.000:1.060
	6-angle DLS	W0	305/877	0.003/0.099	1.000:1.101
		W1	310/892	0.013/0.084	1.000:0.754
		W2	306/881	0.000/0.096	1.000:1.048

Table 8. Performance indices (*PP*, *E_PP*, and *R_PH*) of the true and recovered PSDs for Sample BE

			PP /nm	*E_PP*	*R_PH*
	True PSD		306/974	0.000/0.000	1.000:2.000
Recovered PSDs	1-angle DLS	W0	187/989	0.389/0.015	1.000:0.384
		W1	243/920	0.206/0.055	1.000:0.200
		W2	289/954	0.056/0.021	1.000:0.420
	3-angle DLS	W0	280/950	0.085/0.025	1.000:1.758
		W1	454/761	0.484/0.219	1.000:1.676
		W2	270/617	0.118/0.367	1.000:2.285
	6-angle DLS	W0	235/1012	0.232/0.039	1.000:0.838
		W1	310/983	0.013/0.009	1.000:1.065
		W2	305/978	0.003/0.004	1.000:1.641

Table 9. Performance indices (*PP*, *E_PP*, and *R_PH*) of the true and recovered PSDs for Sample CE

			PP /nm	*E_PP*	*R_PH*
	True PSD		300/502	0.000/0.000	5.000:1.000
Recovered PSDs	1-angle DLS	W0	370/660	0.233/0.315	1.346:1.000
		W1	370/630	0.233/0.255	2.289:1.000
		W2	360/620	0.200/0.235	3.251:1.000
	3-angle DLS	W0	260/490	0.133/0.024	1.678:1.000
		W1	280/520	0.067/0.036	1.661:1.000
		W2	290/510	0.033/0.016	2.113:1.000
	6-angle DLS	W0	280/500	0.067/0.004	2.953:1.000
		W1	290/520	0.033/0.036	3.726:1.000
		W2	300/510	0.000/0.016	4.914:1.000

8. Conclusions

Under some conditions, particularly with bimodal samples, the resolution of the DLS particle sizing measurement is limited by the noise mixed in the ACF data and the inherently lower information content of the data, as well as low PSD information utilization during the inversion process. Generally, the effect of noise can be reduced by optimizing the DLS measurement system and more robust PSD information can be provided by MDLS. A method to effectively extract and make the best use of the PSD information hiding in the noisy data is critical for PSD recovering methods.

MDLS can provide more PSD information than SDLS and, hence improve the measurement of bimodal PSDs. However, this improvement is restricted by the data inversion

routine. Incorporating weighting by the noise distribution, the WCR method can enhance the ability to restrain the noise in ACF data and further improve the measurement. However, the improvement is still limited by the scarce utilization of PSD information during the inversion process.

This paper shows that there are distinct and significant advantages for recovering bimodal PSDs with IWCR data analysis combined with MDLS. The IWCR method can enhance utilization of the PSD information in the ACF data, and effectively weaken the noise in the ACF data at large delay time. Consequently, the IWCR method can provide considerably more accurate PSDs than other common CR methods, and is more able to resolve closely spaced components. By using this method, an accurate PSD recovery is possible for a peak position ratio of 1.2:1, containing large particles ($\geq$ 350nm).

Funding